Rare Metal Materials and Engineering
Volume 50, Issue 7, July 2021
Available online at www.rmme.ac.cn

Science Press

Cite this article as: Zhang Yunsheng, Yang Zhengzheng, Zhou Ge, et al. Thermocompression Deformation Behavior and Mechanism of Ni60Ti40 Alloy[J]. Rare Metal Materials and Engineering, 2021, 50(07): 2385-2392.

ARTICLE

Thermocompression Deformation Behavior and Mechanism of Ni60Ti40 Alloy

Zhang Yunsheng[1], Yang Zhengzheng[1], Zhou Ge[1], Zhang Haoyu[1], Chen Lijia[1], Guan Lei[2]

[1] School of Materials Science and Engineering, Shenyang University of Technology, Shenyang 110870, China; [2] AECC Beijing Institute of Aeronautical Materials, Beijing 100095, China

Abstract: The high-temperature deformation behavior of Ni60Ti40 alloy and the related mechanisms were investigated by thermocompression simulation experiments. The results of high-temperature compression tests were analyzed to reveal the effects of deformation temperature and strain rate on the structural properties and microstructure of alloys. Subsequently, the changing laws of the strain rate sensitivity index m, and the activation energy Q of alloys under different deformation conditions were obtained by calculation. Thermal processing maps based on the dynamic material model and the deformation mechanism maps revealing the dislocation quantity were plotted based on five plastic instability criteria, namely, Prasad, Gegel, Malas, Murty, and Semiatin, to analyze the physical significance of the parameters. The preferred forming zone and the rheological instability zone of the alloys were predicted using the thermal processing theories. The dislocation evolution laws and deformation mechanisms of the grain size with Burgers vector compensation were reported. With the aid of deformation maps, the rheological stress combined with modulus compensation during the high-temperature superplastic deformation was predicted.

Key words: high-strength shape memory alloy; NiTi alloy; dynamic recrystallization; thermocompression simulation experiment; thermal processing map; thermal deformation microstructure

Nickel-titanium-based shape memory alloys (SMAs) with superior properties, such as high specific strength, good mechanical characteristics, excellent shape memory effect, and improved hyperelasticity, are widely-preferred materials for aerospace, military, and defense applications[1-3]. In recent years, the SMA-driven smart inlet has been proven to be an efficient tool to improve the thrust of aircraft engines. The core principle of this method is to completely utilize the shape memory effect of SMAs to efficiently modify the inlet capture zone and the duct lip shapes, which significantly improves the air inlet effect and thereby the thrust, resulting in the fuel conservation. In this regard, numerous researchers have conducted studies to improve the composition, design, synthesis, microstructural features, mechanical characterization, and thermal forming capability of binary Ni-Ti-based SMAs.

Zhang et al[4] prepared a nearly equiatomic Ni50.7Ti49.3 SMA using vacuum induction melting coupled with secondary remelting, subjected the alloy to hot compression experiments at 700~1050 °C and strain rate of 0.01~7.8 s^{-1}, and built a Jonas rheological stress mathematical model. Using this mathematical model, Jiang et al[5] studied the dynamic recovery and dynamic recrystallization (DRX) of alloy within 600~1000 °C and reported the effects of critical deformation quantity on the sizes of DRX grains. Subsequently, Bahador et al[6] reported the structural performance of Ni50.7Ti49.3 SMA during forging and observed significant improvement in its mechanical properties and hyperelasticity. Northwest Institute for Non-ferrous Metal Research of China prepared Ni55Ti45 SMA by varying Ni concentration and noticed significant improvement in the strength of the binary Ni-Ti SMA. Aliakbar et al[7] characterized the DRX behavior of hot compressed Ni55Ti45 alloy using scanning electron microscopy (SEM). With the assistance of hot processing maps, Jong et al[8] predicted the optimal processing range for Ni55Ti45 alloy in hot deformation, compared with that of Ni50.7Ti49.3 SMAs. The increase in Ni concentration results

Received date: July 07, 2020
Foundation item: Natural Science Foundation of Liaoning (2019-ZD-0211)
Corresponding author: Zhou Ge, Ph. D., Professor, School of Materials Science and Engineering, Shenyang University of Technology, Shenyang 110870, P. R. China, E-mail: zhouge@sut.edu.cn

in a reduction of the hot deformation range, which causes that the Ni55Ti45 alloy is prone to local flow, adiabatic shear, mechanical instability, and other rheological instability issues during hot deformation[9,10]. This observation confirms that the increase in Ni concentration leads to the degradation of thermal processing performance. Kaya et al[11] prepared high-strength Ni60Ti40 SMA by further increasing the Ni mass fraction from 55% to 60%. Because of the precipitation hardening effect caused by Ni_3Ti and Ni_2Ti phases, the mechanical strength of Ni-Ti SMA improves. However, the abundant precipitated phases narrow the thermal process window, which causes non-uniform deformation and even cracking during the forging of large construction parts. To date, few studies have been made to overcome this restriction in the practical application of novel high-strength binary Ni-Ti SMAs.

Hence, in this study, the novel high-strength Ni60Ti40 SMA was studied through hot compression deformation experiments with different temperatures and strain rates. The behavior of alloys on basis of the hot compression deformation, energy dissipation/redistribution, and dislocation motion laws were investigated. The suitable process parameters and reported appropriate deformation mechanism for Ni60Ti40 alloys were studied by dynamic material modeling, hot processing maps, and the deformation mechanism maps involving dislocation quantity. The results provide theoretical support for the process optimization, structural stability, control, and defect prevention during hot forming of the novel high-strength Ni60Ti40 SMAs.

1 Experiment

The tested material was the novel high-strength Ni60Ti40 SMA consisting of 60wt% Ni, 39.836wt% Ti, 0.016wt% C, 0.025wt% N, and 0.123wt% O.

The dimension of Ni60Ti40 SMA for the hot compression experiments was Φ8 mm×12 mm. A deep groove of 0.2 mm in depth was made at both ends of specimens. Then the specimens were subjected to single-pass high-temperature compression simulation tests under vacuum atmosphere in a Gleeble-3800 thermo-mechanical simulation system. The deformation temperature changed between 950~1100 °C with an interval of 50 °C. The strain rate varied as 0.005, 0.05, 0.5, and 10 s^{-1}, and the strain capacity was maintained at 0.7. After heat preser-vation for 3 min, the specimens were water-quenched to retain the high-temperature microstructures.

Double-jet experiments were conducted using a Tenupol-5 double-jet equipment with a double-jet solution consisting of nitric acid and methanol with the ratio of 1:3. The experiments were conducted by applying a potential difference of 15 V at -20 °C. The specimens subjected to double-jet tests were prepared for electron microscopy using a GL-6960 ion thinning instrument set at low angle of 3°~4° for 30 min. The specimens were observed under a JEM-2100 transmission electron microscope (TEM). Subsequently, the electron backscatter diffraction (EBSD) patterns of the deformed alloys were recorded using a Gemini 300 SEM equipped with a Nordlys Nano probe. Consequently, the orientation maps under different deformation conditions were obtained, and the crystal grain size distributions were statistically determined.

2 Results and Discussion

2.1 Mechanical properties and high-temperature deformation behavior of Ni60Ti40

The high-temperature compression simulation on Ni60Ti40 specimens was conducted under the condition of temperature 950~1100 °C, strain rate 5×10^{-3}~10 s^{-1} and strain capacity 0.7. The stress (σ)-strain (ε) curves of the Ni60Ti40 alloy under different deformation conditions are shown in Fig. 1. Evidently, the rheological stress σ during high temperature deformation increases with increasing the strain rate. The relationship between σ and strain capacity ε represents the typical behavior of work hardening, softening, and stabilization.

The stress-strain curve corresponding to the deformation temperature of 1000 °C and strain rate of 10 s^{-1} was selected for further analysis, as shown in Fig. 2. At high temperature, with the strain of 0.029, the work hardening θ can be calculated by $\frac{\partial\sigma}{\partial\varepsilon}$, which is very severe and larger than 1200 MPa. When the strain ε exceeds the critical DRX strain (ε_c), θ continuously decreases. With further increasing the strain ε, θ approaches to the minimum value before it gradually stabilizes. The work hardening behavior of alloy obeys the Kocks-Mecking model[12], which is confirmed by the rapid enhancement in the rheological stress at the initial stage (zone I) and gradual stabilization after the strain exceeds ε_c. This behavior is a characteristic of dynamic recovery. The rheological stress reaches the peak value at σ_p and then rapidly reduces. The difference between the theoretical rheological stress and the peak stress is calculated as $\Delta\sigma$, which suggests that the softening mechanism (zone II) is dominant by DRX. Moreover, when the strain ε is close to 0.7, the stable stage (zone III) is obtained. Therefore, the softening effect of this alloy during high-temperature deformation can be noticed when the strain is 0.11~0.67. Similarly, the strain ranges relating to the softening effect under the conditions of different strain rates at 1000 °C are determined and listed in Table 1. Evidently, the strain rate sensitivity has a strong influence on the high-temperature deformation softening behavior of this alloy (Table 1).

2.2 Thermal deformation behavior of Ni60Ti40 alloy

In metallic materials, the essential characteristics of thermal deformation obey the Backofen equation[14,15], as follows:

$$\sigma = K\dot{\varepsilon}^m \tag{1}$$

where σ is the rheological stress of thermal deformation, $\dot{\varepsilon}$ is the strain rate, K is a constant decided by material properties, and m is the strain rate sensitivity index. Eq. (1) can be expressed by another form, as follows:

$$m = \frac{\partial(\lg\sigma)}{\partial(\lg\dot{\varepsilon})} \tag{2}$$

During the high-temperature deformation, Ni60Ti40 alloy behaves as a typical strain rate sensitive material. Thus, m is a

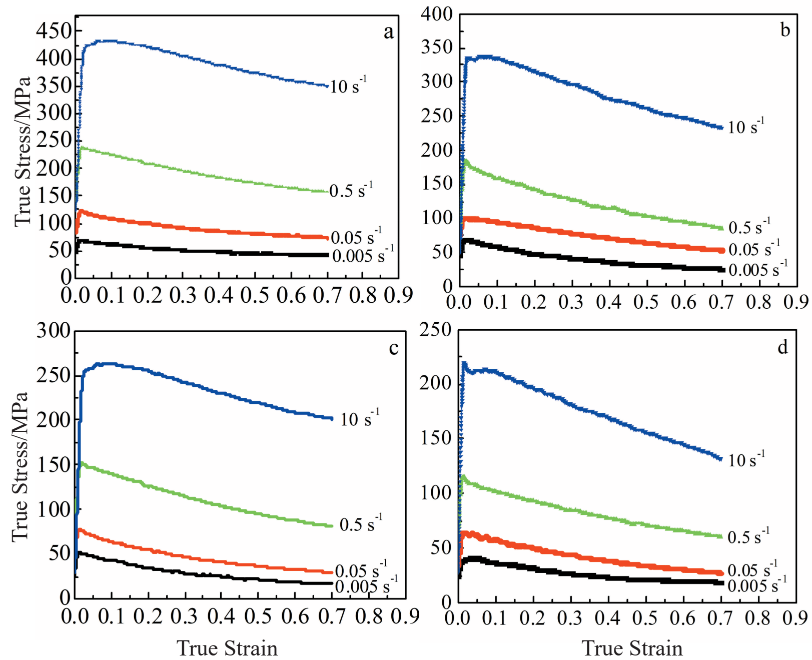

Fig.1 True stress-true strain curves of Ni60Ti40 SMAs under different deformation conditions: (a) 950 °C, (b) 1000 °C, (c) 1050 °C, and (d) 1100 °C

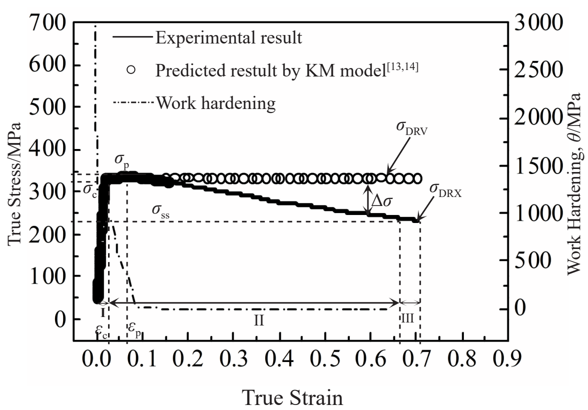

Fig.2 True stress-true strain curve and working hardening curve of Ni60Ti40 alloys (σ_p-peak stress; σ_c-critical stress; σ_{ss}-steady state stress; ε_c-critical strain; ε_p-peak strain)

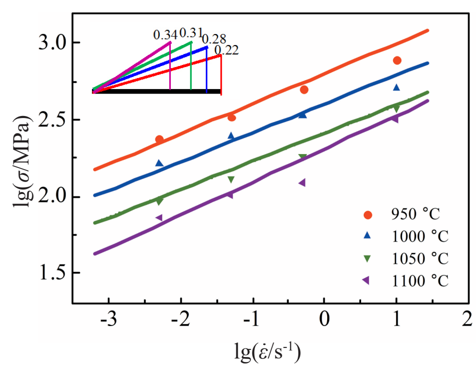

Fig.3 Rheological stress-strain curves of Ni60Ti40 alloy at the strain capacity of 0.7

Table 1 Strain ranges relating to softening mechanism of Ni60Ti40 alloy at 1000 °C

Initial strain rate, $\dot{\varepsilon}$/s^{-1}	5×10^{-3}	5×10^{-2}	0.5	10
ε	0.12~0.49	0.15~0.53	0.17~0.60	0.11~0.67

key parameter to measure the thermoforming performance of the alloy. Fig. 3 shows the rheological stress-strain curves of Ni60Ti40 alloy at 950, 1000, 1050, and 1100 °C and strain capacity of 0.7. The slope of each linear plot yields to the value of m as a function of temperature, as listed in Table 2.

Table 2 Strain rate sensitivity *m* of Ni60Ti40 alloy at different temperatures (ε=0.7)

Temperature/°C	950	1000	1050	1100
m	0.22	0.28	0.31	0.34

Clearly, m of Ni60Ti40 SMA increases with the rise of deformation temperature and the maximum value is 0.34 at 1100 °C. Therefore, the strain rate sensitivity index m of Ni60Ti40 alloy at 950~1100 °C, strain rate of 5×10^{-3}~10 s^{-1}, and strain of 0.7 is 0.22~0.34.

The high-temperature deformation of Ni60Ti40 alloy is a thermally activated process encompassing energy dissipation and redistribution. The relationship among deformation parameters, such as deformation temperature, strain rate, strain capacity, and the rheological stress, can be expressed as follows[15]:

$$\sigma = K\varepsilon^n \dot{\varepsilon}^m \exp\left(\frac{Q}{RT}\right) \tag{3}$$

where n is the processing hardening exponent, Q is the activation energy of deformation, R is the gas constant, and T is the temperature. With a certain strain rate, Eq. (3) can be mathematically simplified as follows:

$$Q = 2.303R\left[\frac{\partial(\lg\sigma)}{\partial(1/T)}\right]_{\varepsilon}\left[\frac{\partial(\lg\dot{\varepsilon})}{\partial(\lg\sigma)}\right]_{T} \tag{4}$$

Fig.4 shows the lgσ-1/T plots of the Ni60Ti40 alloy during high-temperature deformation. From the slopes of the plots shown in Fig. 3 and 4, the terms in Eq. (4), $\left[\frac{\partial(\lg\dot{\varepsilon})}{\partial(\lg\sigma)}\right]_{T}$ and $\left[\frac{\partial(\lg\sigma)}{\partial(1/T)}\right]_{\varepsilon}$, can be calculated. These values are used to calculate the Q values with the strain of 0.7, as shown in Table 3. Therefore, the activation energy of deformation is 248.21~422.78 kJ·mol^{-1}.

Fig. 5 shows the curves corresponding to the hot deformation activation energy Q and the strain rate sensitivity index m for Ni60Ti40 alloy as a function of the deformation temperature. It is observed that Q reduces whereas m increases with the rise of deformation temperature. The materials with m >0.3 possess better hot working performance. This behavior is generally attributed to the DRX of grain boundary slip which achieves the equiaxed grain crystallization[16]. In this study, during the hot deformation at temperatures >1050 °C, when m of the alloy is larger than 0.3, the deformed microstructures are typical of equiaxed post-DRX, as shown in Fig.6, and the

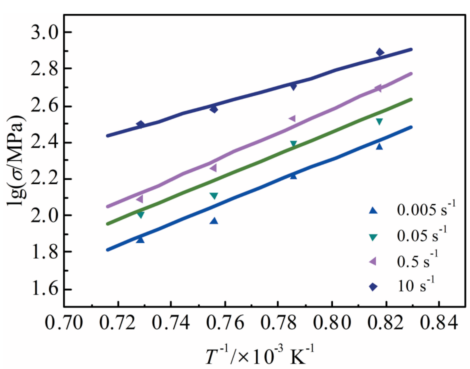

Fig.4 Relationship between lgσ and 1/T of Ni60Ti40 alloy

Table 3 Activation energy Q of Ni60Ti40 alloy during thermal deformation with ε=0.7 (kJ·mol^{-1})

$\dot{\varepsilon}$/s^{-1}	Temperature/°C			
	950	1000	1050	1100
5×10^{-3}	422.78	385.76	358.24	307.89
5×10^{-2}	358.15	335.40	301.58	288.25
0.5	315.15	298.40	278.23	269.25
10	300.24	281.03	264.22	248.21

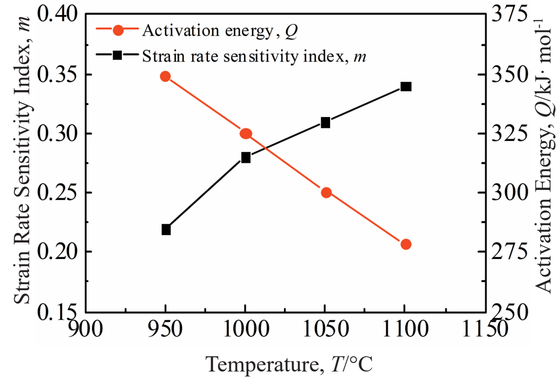

Fig.5 Hot deformation activation energy Q and strain rate sensitivity index m as a function of temperature T for Ni60Ti40 alloy

Q value at this temperature is 300.57 kJ·mol^{-1}. The experiments on the Ni50.7Ti49.3 SMA reported by Beijing University of Science and Technology showed that the Q value is 185.48~209.35 kJ·mol^{-1} [17]. Reportedly, the Q value for binary Ni-Ti SMAs increases with raising the Ni concentration, which largely affects the microstructure evolution mechanism of alloys during hot deformation.

2.3 Thermal processing map of Ni60Ti40 alloy

The rheological instability criteria during the thermal deformation of metallic materials were investigated. The Prasad, Gegel, Murty, Malas, and Semiatin instability criteria are of significance to processing maps. Based on the energy dissipation theory, Prasad et al[18] divided the system energy (P) during metallic thermal deformation into dissipation energy (G) and dissipation assisting energy (J), which can be expressed as follows:

$$P = \sigma\dot{\varepsilon} = G + J = \int_0^{\dot{\varepsilon}} \sigma \mathrm{d}\dot{\varepsilon} + \int_0^{\sigma} \dot{\varepsilon}\mathrm{d}\sigma \tag{5}$$

On basis of the theoretical derivation and mathematical conversion, a dimensionless parameter η reflecting the energy dissipation and redistribution during thermal deformation is proposed as follows:

$$\eta = \frac{J}{J_{\max}} = \frac{2m}{m+1} \tag{6}$$

The Prasad instability criterion based on the maximum entropy production rate is expressed as follows:

$$\xi(\dot{\varepsilon}) = \frac{\partial \ln\left(\frac{m}{m+1}\right)}{\partial \ln\dot{\varepsilon}} + m < 0 \tag{7}$$

Based on the fundamentals of the second law of thermodynamics, Gegel completely considered the relationship between rheological instability and the temperature sensitivity parameters[19]. The Gegel instability criterion is proposed as follows:

$$\frac{\partial\eta}{\partial(\ln\dot{\varepsilon})} > 0, \frac{\partial m}{\partial(\ln T)} < 0 \tag{8}$$

On basis of the Gegel criterion, Malas et al[20] introduced the

Liapunov function $L(\eta, s)$ and proposed the Malas instability criterion as follows:

$$\frac{\partial m}{\partial(\ln\dot{\varepsilon})} > 0, \frac{\partial m}{\partial(\ln T)} < 0 \tag{9}$$

Murthy et al[21] modified the Prasad instability criterion to model the strain rate sensitivity index m, as given in Eq.(10):

$$2m < \eta \tag{10}$$

Subsequently, combined with Eq. (11), the Murthy instability criterion suitable for any stress-strain velocity curve can be deduced, as presented in Eq.(12):

$$\eta = \frac{J}{J_{\max}} = \frac{2J}{\sigma\dot{\varepsilon}} \Rightarrow \frac{\mathrm{J}}{\dot{\varepsilon}} = \frac{1}{2}\eta\sigma \tag{11}$$

$$J = \int_0^\sigma \dot{\varepsilon}\mathrm{d}\sigma \Rightarrow \frac{\partial J}{\partial\dot{\varepsilon}} = \frac{\partial\sigma}{\partial\dot{\varepsilon}}\dot{\varepsilon} = \sigma\frac{\partial\ln\sigma}{\partial\ln\dot{\varepsilon}} = m\sigma \tag{12}$$

Semiatin et al[22] defined the parameters according to the force balance method and proposed a mobile instability criterion:

$$\alpha = \frac{\mathrm{d}\dot{\varepsilon}}{\dot{\varepsilon}\mathrm{d}\varepsilon} = \left(-\frac{\mathrm{d}\sigma}{\sigma\mathrm{d}\varepsilon}\right)\frac{1}{m} = -\frac{\gamma}{m} \quad (\alpha > 5) \tag{13}$$

In this study, the characteristics of Ni60Ti40 alloy during high-temperature thermal deformation based on the abovementioned instability criteria are presented in Fig. 6. The changes of the power dissipation rate can be expressed by the contour curves, and the dashed areas correspond to the rheological instability zones.

As shown in Fig. 6, the rheological instability criteria in Ni60Ti40 are valid at the upper left and lower right regions of the processing map. The temperature at the upper left region is 950~985 °C and the strain rate range is 0.5~10 s^{-1}. The

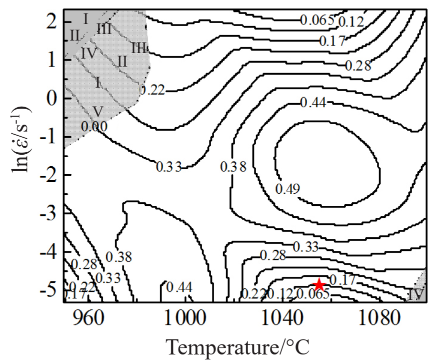

Fig. 6 Thermal processing map of different instability criteria for Ni60Ti40 alloy (I-Prasad; II-Gegel; III-Malas; IV-Murty; V-Semiatin)

rheological instability complies with all the mentioned instability criteria. The microstructure of the deformed alloy is shown in Fig. 7a for comparison. Cracks are prominent in the microstructure of deformed alloy. The presence of cracks is due to the very large strain rate and the heat generated during high-temperature deformation, resulting in the formation of insulated shear zones inside the crystal grains. The superimposition and enrichment of numerous insulated shear zones lead to the formation of insulated shear cracks inside the crystal grains. Consequently, the forming performance of the alloy at low-temperature and high strain rate is recorded to

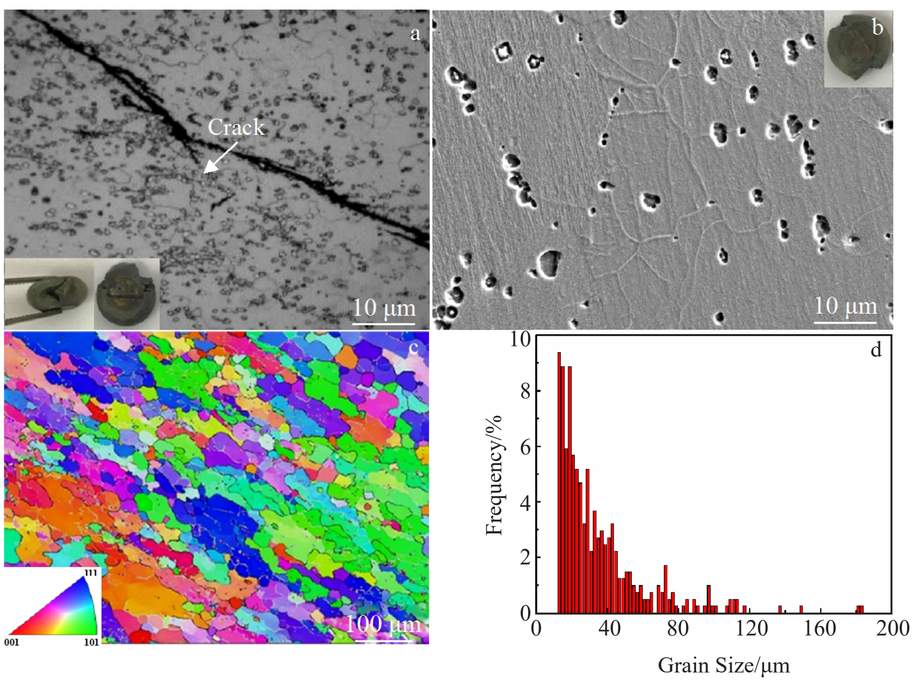

Fig.7 Microstructures of Ni60Ti40 alloy under different deformation conditions: (a) 900 °C, 10 s^{-1} and (b) 1100 °C, 5×10^{-3} s^{-1}; EBSD map of deformed Ni60Ti40 alloy at 1050 °C and strain rate of 5×10^{-3} s^{-1} (c); grain size distribution of Ni60Ti40 alloy (d)

be poor. At the lower right region of the processing map where the temperature is 1080~1100 °C and strain rate is 5×10^{-3}~7.2×10^{-3} s^{-1}, the rheological instability is calculated to be consistent with Murty criterion (zone IV). The corresponding microstructure of the deformed alloy is shown in Fig. 7b. Because of the high deformation temperature, phase transformation occurs during the deformation. Cavities appear at the phase boundary because of the stress concentration at the phase interface due to prolonged exposure to external force. As the temperature increases to 1100 °C, the diffusion accelerates, leading to the expansion of cavities at the phase boundary and reducing the high-temperature forming performance of this alloy. However, at the region of temperature between 1040~1070 °C and the strain rate between 5×10^{-3}~7.2×10^{-3} s^{-1}, the power dissipation rate η is significantly large and shows the absence of rheological instability. The corresponding EBSD map of the deformed alloy is shown in Fig.7c.

The white and black lines in Fig. 7c represent small angle grain boundaries (2°~15°) and large angle grain boundaries (>15°), respectively. Different colors represent different grain orientations. The grains with size of 100~200 μm account for a small proportion (Fig. 7d). These grains representing the original crystal possess clean interior and exhibit a clearly straight grain boundary. The grains with size <40 μm account for the largest proportion (Fig.7d). These grains exhibit abundant small angle boundaries and bent grain boundaries, representing the newly formed DRX grains during the hot deformation. The grains with size of 40~100 μm show a few small angle boundaries in their interior region. The grain boundary is straight and uniform. This part of crystal grains may grow up after DRX. The microstructural features prove that the Ni60Ti40 alloy experiences significant DRX during hot deformation under the process conditions.

Evidently, DRX occurs during the hot deformation, as manifested by the uniform grains in the microstructure. Compared with the microstructure of original grains, the DRX-generated grains are significantly refined and moderately equiaxed. In addition, no insulated shear cracks or cavities can be observed in the microstructure. Thus, the Ni60Ti40 alloy possesses excellent forming properties during hot deformation in this zone.

2.4 Deformation mechanism of Ni60Ti40 with dislocation concentration

Based on the Ruano-Wadsworth-Sherby (RWS) deformation mechanism, a dislocation model was constructed through a constitutive equation. Thereafter, the deformation mechanism maps showing the concentration of dislocation, grain size, strain rate, and rheological stress are presented.

2.4.1 Construction of deformation mechanism

The high temperature deformation of metals can be described by Eq.(14) as follows[23,24]:

$$\dot{\varepsilon}_i = A_i\left(\frac{b}{d_i}\right)^p \frac{D}{KTb^2}\left(\frac{\sigma_i}{E}\right)^n \tag{14}$$

where n and p are material constants; σ_i is the stress; $\dot{\varepsilon}_i$ is the steady-state strain rate; E is Young's modulus; d_i is the grain size; b is the Burgers vector; D is the diffusion coefficient comprising the lattice diffusion coefficient D_L and the crystal boundary diffusion coefficient D_{gb}; A_i is constant; K is Boltzmann constant.

The internal dislocation root count of single-crystal grains can be computed by Eq.(15) as follows[25]:

$$n_i = 2\left[(1-v)\pi d_i \tau_i\right]/(Gb) \tag{15}$$

where n_i is the internal dislocation root count inside crystal grains, v is Poisson's ratio, and τ_i=0.5σ_i is the shear stress (MPa). The compression test results of Ni60Ti40 alloy at 1050 °C (Table 4) are substituted into Eq.(14) and Eq.(15) to solve the constitutive equation. Furthermore, the crystal grain sizes of the included dislocation count underlying the RWS deformation mechanism are presented (Fig.8) with consideration of the modulus compensation stress along X axis and the Burgers vector compensation along Y axis.

2.4.2 Application of deformation mechanism

The normalized grain size of Burgers vector compensation of $(d/b)\times10^7$ and the normalized flow stress of modulus compensation of $(\sigma/E)\times10^4$ for Ni60Ti40 alloy at 1050 °C are listed in Table 5.

The deformation of Ni60Ti40 alloy at 1050 °C and strain rate of 5×10^{-3}~10 s^{-1} is encompassed by the dislocation polygons (3.75×10^7) (367) (2460) (3258) (28 657) and (3.75×10^7) (8.75×10^8) (58) (19) (367) (Fig. 8 and Table 5). During the deformation process, with the increment in strain rate, the mechanism transforms from the grain boundary slide (con-

Table 4 Physical parameters of Ni60Ti40 alloys[26~28]

Parameter	Value
b/m	2.15×10^{-10}
k/J·K^{-1}	1.38×10^{-23}
D_L at 1050 °C/m^2·s^{-1}	9.09×10^{-10}
E/MPa	6.57×10^5
v	0.31
D_{gb} at 1050 °C/m^2·s^{-1}	4.34×10^{-9}

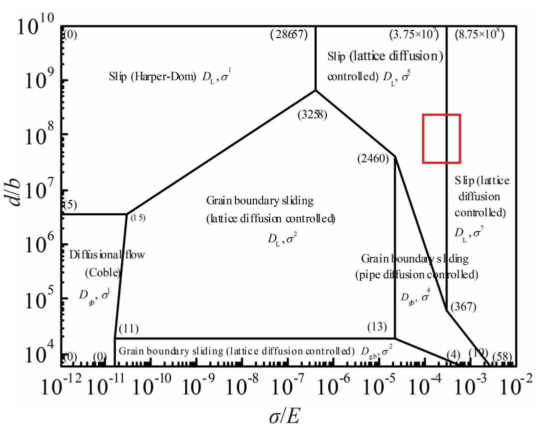

Fig.8 Rate controlling deformation mechanism map for Ni60Ti40 alloy

Table 5 Normalized grain size and flow stress of deformed Ni60Ti40 alloy

Deformation temperature, T/°C	Normalized grain size with Burgers vector compensation, $(d/b)\times10^{-7}$	Normalized flow stress with modulus compensation, $(\sigma/E)\times10^{4}$	Strain rate $\dot{\varepsilon}/\times10^{-4}$ s^{-1}
1050	7.2~14.7	2.5~12.5	50~10^5

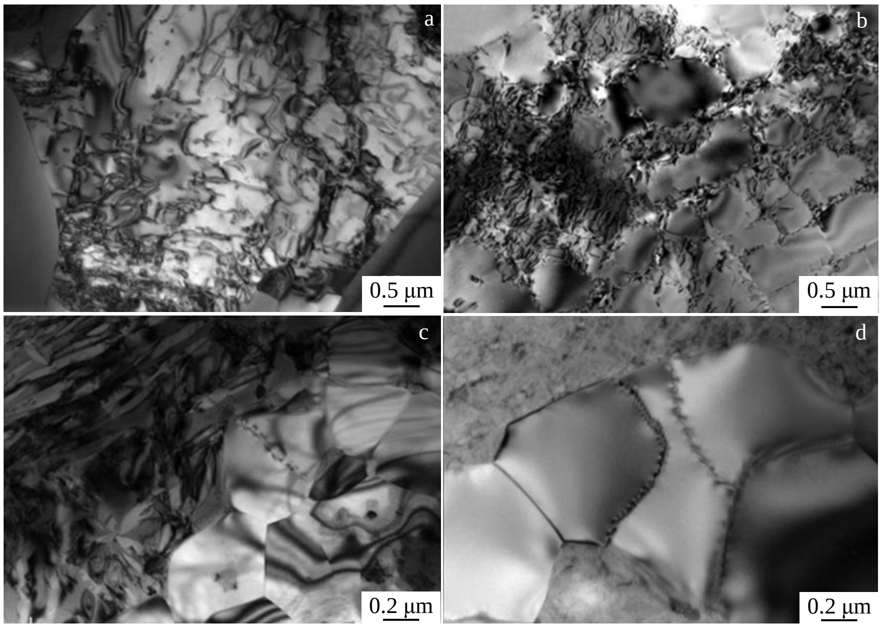

Fig.9 TEM images of Ni60Ti40 alloy with ε=0.7 at different strain rates: (a) 10 s^{-1}, (b) 0.5 s^{-1}, (c) 0.05 s^{-1}, and (d) 5×10^{-3} s^{-1}

trolled by lattice diffusion with stress exponent of 5) to dislocation glide (controlled by lattice diffusion with stress exponent of 7).

Fig.9 shows the TEM images of Ni60Ti40 alloy at 1050 °C, and strain rate of 5×10^{-3}~10 s^{-1}. At the strain rate of 10 s^{-1}, the extensive dislocation or interaction inside crystal grains can be observed. The dislocation is manifested by slip or cross-slip, which generates dislocation tangling or dislocation cells. As the strain rate reduces, the dislocation motion intensifies, presenting the formation of extensive dislocation defects inside the crystals, which leads to changes in the lattices, and further induces grain boundary slip controlled by lattice diffusion (Fig. 9b). When the strain rate continually reduces, the dislocation motion continues to thrive, resulting in an extensive residual dislocation interaction at grain boundary. This interaction promotes the generation of large angle grain boundaries. In addition, because of grain boundary slip, the DRX nucleation and growth gradually occur, resulting in the formation of equiaxed grains (Fig.9c and 9d).

3 Conclusions

1) The strain rate sensitivity index m of Ni60Ti40 alloy at 950~1100 °C, strain rate of 5×10^{-3}~10 s^{-1}, and strain of 0.7 is computed as 0.22~0.34. The activation energy of deformation is calculated as 248.21~422.78 kJ·mol^{-1}.

2) The thermal processing performance of Ni60Ti40 during high temperature compression was predicted based on five instability criteria (Prasad, Gegel, Malas, Murty, and Semiatin) and represented on processing map. The suitable processing and forming conditions are 1040~1070 °C and strain rate of 5×10^{-3}~7.2×10^{-3} s^{-1}.

3) The Ruano-Wadsworth-Sherby deformation mechanism map of Ni60Ti40 involving dislocation quantity was determined, and the high temperature deformation mechanisms at 1050 °C and different strain rates were predicted.

References

1 Schetky L M D. *Materials Science Forum*[J], 2000, 327: 9
2 Kainuma R, Imano Y. *Nature*[J], 2006, 439: 957
3 Ni D K, Wang J J. *J Mater Sci Technol*[J], 2016, 32(2): 162
4 Zhang W H, Zhang S H. *Acta Metallurgica Sinica*[J], 2006, 42(10): 1036
5 Jiang S Y, Zhang Y Q, Zhao Y N *et al. Trans Nonferr Metal Soc*[J], 2013, 23(1): 140
6 Bahador A, Hamzah E, Kondoh K *et al. Trans Nonferr Metal Soc*[J], 2018, 28(3): 502
7 Aliakbar K, Kamran D. *Metall Mater Trans A*[J], 2010, 41(10): 2595
8 Jong T Y, Jeoung H K. *Mater Res Bull*[J], 2014, 58: 234
9 Jiang S Y, Zhang Y Q. *Trans Nonferr Metal Soc*[J], 2012,

22(1): 90
10 Huang X, Liu Y. *Scr Mater*[J], 2001, 45(2): 153
11 Kaya I. *Smart Mater Struct*[J], 2016, 25(12): 125 031
12 Bussiba A, Artzy A. *Mater Sci Eng A*[J], 2001, 302(1): 56
13 Lin Y C, Chen X M, Wen D X *et al. Science Comput Mater Sci*[J], 2014, 83: 282
14 Tan L M, Li Y P, Liu F *et al. Mater Sci Technol*[J], 2019, 35(11): 2591
15 Eleti R R, Bhattacharjee T. *Acta Mater*[J], 2019, 171: 132
16 Wu L H, Jia C L, Han S C *et al. J Alloy Compd*[J], 2019, 787: 1320
17 Deng H B, Chen Y H, Li S H *et al. Materials & Design*[J], 2020, 189: 108 491
18 Prasad Y V, Seshacharyulu R K. *Transactions of International Materials Review*[J], 1998, 43(6): 243
19 Prasad Y V R K, Gegel H L. *Metall Trans*[J], 1984, 15(10): 1883
20 Malas J C, Seetharaman V. *JOM*[J], 1992, 44(6): 8
21 Murty S V S N, Rao B N. *Materials Science and Engineering A*[J], 1998, 254(1-2): 76
22 Semiatin S L, Lohoti G D. *Metall Trans A*[J], 1983, 14(1): 105
23 Kawasaki M, Langdon G. *Mater Sci Eng A*[J], 2011, 528(19-20): 6140
24 Umemoto M, Hiramatsu A. *ISIJ Int*[J], 1992, 32(3): 306
25 Liu C, Zhou G, Wang X *et al. Materials*[J], 2019, 12(21): 3520
26 Chen Y C, Molnárová O, Tyc O *et al. Acta Materials*[J], 2019, 180: 243
27 Hou Q Y, Wang J T. *Adv Mater Res*[J], 2010, 146: 225
28 Kawasaki M, Langdon T G. *Mater Sci Eng A*[J], 2011, 528(19-20): 6140

Ni60Ti40合金热压缩变形行为及机理

张允胜[1]，杨丁丁[1]，周　舸[1]，张浩宇[1]，陈立佳[1]，官　磊[2]
(1. 沈阳工业大学 材料科学与工程学院，辽宁 沈阳 110870)
(2. 中国航空发动机集团公司北京航空材料研究院，北京 100095)

摘　要：对Ni60Ti40合金高温变形行为及变形机理进行了研究。通过计算获得了该合金在不同变形工艺下的应变速率敏感性指数m和变形激活能Q的变化规律，分别构建了Prasad、Gegel、Malas、Murty和Semiatin等不同失稳判据下的动态材料模型热加工图及包含位错数量的变形机理图。应用热加工图理论分析了该合金的适合成形加工区和流变失稳区，运用变形机理图预测了该合金高温变形过程中基于柏氏矢量补偿的晶粒尺寸和基于模量补偿的流变应力下的位错演变规律及高温变形机理。

关键词：高强度形状记忆合金；NiTi合金；动态再结晶；热压缩模拟实验；热加工图；热变形组织

作者简介：张允胜，男，1998年生，硕士生，沈阳工业大学材料科学与工程学院，辽宁 沈阳 110870，E-mail：zys086415@163.com